Nonlinear dynamics of double-cavity optical bistability of a three-level ladder system

H. Aswath Babu and Harshawardhan Wanare
Department of Physics, Indian Institute of Technology Kanpur, Kanpur 208016, India
(Received 8 September 2010; published 18 March 2011; publisher error corrected 24 March 2011)

We present nonlinear dynamical features of two-photon double-cavity optical bistability exhibited by a three-level ladder system in the mean-field limit at low input light levels. The system exhibits a hump-like feature in the lower branch of the bistable response, wherein a region of instability develops. The system displays a range of dynamical features varying from normal stable switching to periodic self-pulsing and chaos. The inclusion of two competing cooperative atom-field couplings leads to such rich, nonlinear dynamical behavior. We provide a domain map that clearly delineates the various regions of stability, as well as bifurcation diagrams with associated supporting evidence that identifies the period-doubling route to chaos.

DOI: 10.1103/PhysRevA.83.033819 PACS number(s): 42.65.Pc, 42.65.Sf, 42.50.Gy

I. INTRODUCTION

Understanding instability is pivotal to fabricating practical devices. In recent times chaos has been used in a variety of applications including generating random numbers [1,2], obtaining ultrawide bandwidths [3], and in optical communication schemes [4,5]. An all-optical implementation of nonlinear dynamical behavior is preferred, as it offers a larger bandwidth (greater than a few gigahertz [5]) in comparison to systems involving electronic circuits that have a limited bandwidth ($\sim$100 kHz); moreover, all-optical systems are largely immune to thermal noise. The phenomenon of all-optical bistability [6,7] has historically offered a fertile platform for studying nonlinear dynamical effects [8–10]. In this paper we describe an all-optical bistable system that is simple yet exhibits a variety nonlinear dynamical behavior within physically accessible regimes.

In conventional optical bistability (OB), nonlinear dynamics arises due to the atom coupling to many cavity modes [11,12]. A two-level atomic system interacting with a single mode does not exhibit chaos unless driven much above the saturation intensity levels [7]. We consider a system wherein nonlinear dynamics arises due to the interplay of cooperative atom-cavity coupling at two different frequencies along two transitions within the atom. This results in a hitherto unseen nonlinear dynamical regime that arises in double-cavity two-photon OB, where both fields experience independent feedback. This new regime occurs at low input light levels, and the system also exhibits negative as well as positive hysteresis [13]. We undertake a systematic study of the phase-space structure that allows us to selectively *steer* the system to exhibit either stable periodic self-pulsing or chaos. Such control mechanisms offer the possibility of utilizing these dynamics for communication technologies involving multiwavelength operation, apart from the fact that this simple system also offers a different paradigm for study of the fundamental aspects of optical instabilities.

We review some of the earlier works in order to place this study in the proper context. Optical instability in OB has been extensively studied in the last four decades, since the pioneering work by Ikeda *et al.* [8], where delayed feedback in an OB system resulted in periodic instabilities and chaotic behavior. Single-mode instabilities ranging from gain-based laser systems [14] to passive two-level optical bistable systems have also been investigated earlier [15,16]. Various studies related to the three-level atoms interacting with multiple fields leading to chaos have been undertaken: Savage *et al.* [17] described the possibility of tri- and quadrastability as well as self-pulsing and chaos; Grangier *et al.* [18] have studied OB in the purely dispersive limit and shown the occurrence of chaos for high field intensities. Chaos has also been demonstrated in a three-level Λ system with only the probe field experiencing feedback; coupling-field detuning is used to drive the system to chaos at high input intensities [19]. To the best of our knowledge, the OB regime we describe has not been reported earlier; we obtain chaos for moderate cooperative parameters in the lower branch of the bistable response at low input intensity levels. These effects arise due to the competition between the two cooperative branches within the atom. The effects are quite robust and occur over a wide parameter regime; moreover, no approximations are made with regard to the nonlinearity of the active medium. This model is ideal for investigation of optical chaos, as it arises just beyond the single-mode limit; we consider here only two independent single modes associated with the two monochromatic fields coupling to three-level atoms. The system exhibits coordinated dynamics at the two distinct optical frequencies.

The organization of the paper is as follows: In Sec. II we present the description of the theoretical model. We provide a detailed stability domain map as well as the details of the numerical modeling in Sec. III. In Sec. IV we present the results and analysis of the nonlinear dynamical features including bifurcation diagrams, spectra, and phase-space plots. We conclude in Sec. V.

II. THEORETICAL MODEL

We consider two optical fields in two independent unidirectional ring cavities that share an overlapping region containing a collection of three-level atoms of number density N, as shown in Fig. 1. The electric field associated with the optical fields at the atom is given by

$$E = E_1 e^{i\omega_1 t} + E_2 e^{i\omega_2 t} + \text{c.c.}, \tag{1}$$

which consists of two monochromatic fields of amplitude E_1 and E_2, at frequencies ω_1 and ω_2, coupling to the transitions $|1\rangle \leftrightarrow |2\rangle$ and $|2\rangle \leftrightarrow |3\rangle$, having dipole moments d_{12} and d_{23},

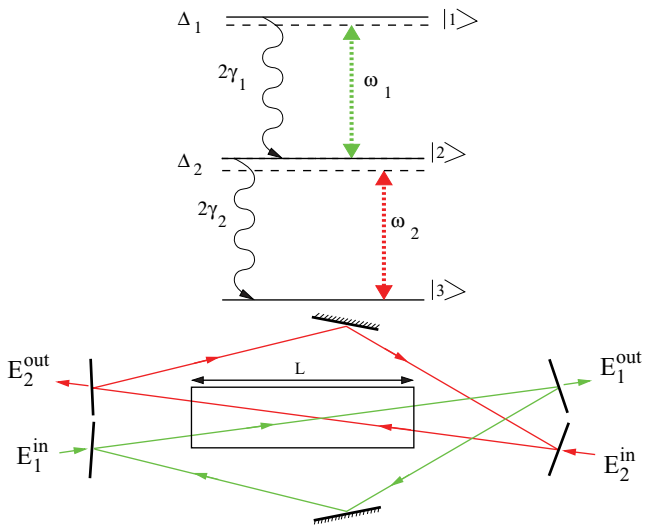

FIG. 1. (Color online) Top: Schematic of the three-level ladder system interacting with the two fields E_1 and E_2 at frequencies ω_1 and ω_2, respectively. Bottom: Double-cavity OB setup, where the active medium contained within the length L interacts with the two fields associated with the two independent unidirectional ring cavities.

respectively. The fields within the active medium are chosen to be counter-propagating to minimize the effects of Doppler broadening in the ladder atomic system.

Our approach closely follows the procedure detailed in Ref. [7]. We consider the following boundary conditions, imposed independently on the two fields due to the cavity feedback, that relate the input-output fields,

$$E_i^{\text{out}}(t) = \sqrt{T_i}\,E_i(L,t), \tag{2}$$

$$E_i(0,t) = \sqrt{T_i}\,E_i^{\text{in}} + R_i e^{-i\delta_i} E_i(L,t-\Delta t), \tag{3}$$

for the field at ω_i. The subscript $i = 1,2$, throughout this paper, refers to the two fields at frequencies ω_1 and ω_2, respectively. Here, T_i and R_i are the transmission and reflection coefficients associated with the two independent cavities, and L is the length of the active medium. The cavity detunings are $\delta_i = (\omega_i^c - \omega_i)\mathcal{L}_i/c$, where ω_i^c is the nearest resonant cavity frequency close to the field frequency ω_i, and $\mathcal{L}_i$ is the total length of the cavity. For simplicity, we have assumed that the time taken by both fields outside the active medium is identical and is represented as $\Delta t = (\mathcal{L}_i - L)/c$. The wave equation under the slowly varying envelope approximation is given as

$$\frac{\partial E_i}{\partial t} + c\frac{\partial E_i}{\partial z} = i2\pi\omega_i P(\omega_i), \tag{4}$$

where $P(\omega_i)$ is the macroscopic atomic polarization.

We consider the deviations of the fields from the stationary solutions of Eq. (4) to be

$$\delta E_i(z,t) = E_i(z,t) - E_i^{\text{st}}(z), \tag{5}$$

$$\delta P_i(z,t) = P_i(z,t) - P_i^{\text{st}}(z) \tag{6}$$

upon substituting Eqs. (5) and (6) in Eqs. (3) and (4), and we obtain the equations governing the deviations as

$$\frac{\partial \delta E_i}{\partial t} + c\frac{\partial \delta E_i}{\partial z} = i2\pi\omega_i \delta P(\omega_i), \tag{7}$$

$$\delta E_i(0,t) = R_i e^{-i\delta_i}\delta E_i(L,t-\Delta t). \tag{8}$$

The boundary condition, Eq. (8), can be made periodic in space by the following transformation [7]:

$$\delta\tilde{E}_i(z,t') = W(z,T_i)\;\delta E_i(z,t'), \tag{9}$$

$$\delta\tilde{P}_i(z,t') = W(z,T_i)\;\delta P_i(z,t'), \tag{10}$$

$$W(z,T_i) = \exp\left[\frac{z}{L}\ln\left(R_i e^{-i\delta_i}\right)\right], \tag{11}$$

$$t' = t + \Delta t\frac{z}{L}. \tag{12}$$

Using the above transformation, Eq. (7) can be recast as

$$\frac{\partial \delta\tilde{E}_i}{\partial t'} + c\frac{L}{\mathcal{L}_i}\frac{\partial \delta\tilde{E}_i}{\partial z} = -\kappa_i(1+i\theta_i)\,\delta\tilde{E}_i + i2\pi\omega_i\frac{L}{\mathcal{L}_i}\delta\tilde{P}(\omega_i), \tag{13}$$

with cavity decay $\kappa_i = cT_i/\mathcal{L}_i$ and cavity detuning $\theta_i = \delta_i/T_i$. Note that for $T_i \ll 1$, $\ln(R_i) \approx -T_i$. We undertake the mean-field limit for both fields, that is, $\alpha_i L \to 0$, $T_i \to 0$, and $\delta_i \to 0$, which essentially refers to spatially uniform fields that change little in each pass through the cavity; however, owing to the large cavity photon lifetime, the photons undertake many passes inside the cavity [11], resulting in significant cooperative effects. Integrating Eq. (4) in the steady state and under the mean-field limit, we obtain

$$E_i^{\text{st}}(L) - E_i^{\text{st}}(0) = i2\pi\omega_i\frac{L}{c}P_i^{\text{st}}(\omega_i). \tag{14}$$

The boundary condition, Eq. (3), is used above, and neglecting the terms proportional to powers of $T > 1$, we obtain

$$0 = -i\kappa_i\theta_i E_i^{\text{st}}(L) - \kappa_i\left(E_i^{\text{st}}(L) - \frac{E_i^{\text{in}}}{\sqrt{T_i}}\right) + i2\pi\omega_i\frac{L}{\mathcal{L}_i}P_i^{\text{st}}(\omega_i), \tag{15}$$

which, under the mean-field limit (i.e., E_i^{st} being uniform in space), can be summed up with Eq. (13) to obtain

$$\frac{\partial E_i}{\partial t'} + c\frac{L}{\mathcal{L}_i}\frac{\partial E_i}{\partial z} = -i\kappa_i\theta_i E_i - \kappa_i\left(E_i - \frac{E_i^{\text{in}}}{\sqrt{T_i}}\right) + i2\pi\omega_i\frac{L}{\mathcal{L}_i}P_i(\omega_i). \tag{16}$$

Note also that we have used the fact that $W(z,T) \approx 1$ in the mean-field limit, hence $\delta\tilde{E}_i = \delta E_i$ and $\delta\tilde{P}_i = \delta P_i$.

The above equation is reformulated in terms of dimensionless quantities as

$$\frac{\partial F_i}{\partial t'} + c\frac{L}{\mathcal{L}_i}\frac{\partial F_i}{\partial z} = \kappa_i[-i\theta_i F_i - (F_i - y_i) + i2C_i\tilde{\rho}_{mn}], \tag{17}$$

where the cooperative parameter $C_i = \alpha_i L/2T_i$, and the absorption coefficient $\alpha_i = 2\pi\omega_i|d_{mn}|^2 N/\hbar c\gamma_i$ (the subscripts

m and n denote the corresponding transition involving the atomic levels $|1\rangle$, $|2\rangle$, and $|3\rangle$). The other quantities are

$$F_i = \frac{d_{mn}E_i}{\hbar\gamma_i}, \quad x_i = \frac{d_{mn}E_i^{\text{out}}}{\hbar\gamma_i\sqrt{T_i}}, \quad y_i = \frac{d_{mn}E_i^{\text{in}}}{\hbar\gamma_i\sqrt{T_i}}, \quad P_i(\omega_i) = Nd_{mn}\tilde{\rho}_{mn}. \tag{18}$$

The fields as well as the atomic variables are expanded in the basis of cavity modes ($\omega_i^c + q\Omega_i$, $\Omega_i = 2\pi c/\mathcal{L}_i$ for $q = 0, \pm 1, \ldots$) as

$$F_i(z,t') = \sum_q e^{ik_i^{(q)}z} f_i^{(q)}(t'), \tag{19}$$

$$\tilde{\rho}_{mn}(z,t') = \sum_q e^{ik_i^{(q)}z} \rho_{mn}^{(q)}(t'), \tag{20}$$

where $k_i^{(q)} = 2\pi q/L$ and the functions $\exp[ik_i^{(q)}z]$ obey the periodicity boundary condition. The temporal evolution equation for mode amplitudes $f_i^{(q)}$ is

$$\frac{\partial f_i^{(q)}}{\partial t'} = -iq\Omega_i f_i^{(q)} + \kappa_i\left[-i\theta_i f_i^{(q)} - \left(f_i^{(q)} - y_i\delta_{q,0}\right) + i2C_i\rho_{mn}^{(q)}\right], \tag{21}$$

and under the uniform-field approximation the amplitudes $f_i^{(0)}$,$\rho_{mn}^{(0)}$, corresponding to resonant mode, are nonzero. Thus, using $q = 0$, $f_i^{(0)} = x_i$, and $\rho_{mn}^{(0)} = \rho_{mn}$, we obtain

$$\frac{\partial x_i}{\partial t'} = \kappa_i\left[-x_i(1 + i\theta_i) + y_i + 2iC_i\rho_{mn}\right], \tag{22}$$

where $y_i(x_i)$ represents the normalized cavity input(output) fields.

We now describe the density matrix equation that governs the interaction of the atom with fields:

$$\frac{\partial\rho}{\partial t'} = -\frac{i}{\hbar}[\hat{H},\rho] + \hat{\mathcal{L}}\rho, \tag{23}$$

where the total Hamiltonian $\hat{H}$ is

$$\hat{H} = \hat{H}_{\text{at}} + \hat{H}_{\text{int}}, \quad \hat{H}_{\text{at}} = \hbar\omega_{13}|1\rangle\langle 1| + \hbar\omega_{23}|2\rangle\langle 2|, \quad \hat{H}_{\text{int}} = -\vec{d}\cdot\vec{E} = -\hbar G_1|1\rangle\langle 2| - \hbar G_2|2\rangle\langle 3| + \text{H.c.} \tag{24}$$

The terms $\hbar\omega_{13}(\hbar\omega_{23})$ correspond to the energy levels of the bare atom measured from the ground state $|3\rangle$, and the interaction Hamiltonian $\hat{H}_{\text{int}}$ is given in the dipole approximation, involving the Rabi frequencies:

$$G_1 = \frac{d_{12}E_1}{\hbar}, \quad G_2 = \frac{d_{23}E_2}{\hbar}.$$

Relaxation processes like spontaneous emission and dephasing of the atomic coherence are contained in the Liouville operator $\hat{\mathcal{L}}$ in Eq. (23). We explicitly enumerate the equations of motion of density matrix elements under the rotating-wave approximation:

$$\frac{\partial\rho_{11}}{\partial t'} = -2\gamma_1\rho_{11} + iG_1\rho_{21} - iG_1^*\rho_{12},$$

$$\frac{\partial\rho_{12}}{\partial t'} = -(\gamma_1 + \gamma_2 + i\Delta_1)\rho_{12} + iG_1(\rho_{22} - \rho_{11}) - iG_2^*\rho_{13},$$

$$\frac{\partial\rho_{13}}{\partial t'} = -\left[\gamma_1 + i(\Delta_1 + \Delta_2)\right]\rho_{13} + iG_1\rho_{23} - iG_2\rho_{12},$$

$$\frac{\partial\rho_{22}}{\partial t'} = 2\gamma_1\rho_{11} - 2\gamma_2\rho_{22} - iG_1\rho_{21} + iG_1^*\rho_{12} + iG_2\rho_{32} - iG_2^*\rho_{23}, \tag{25}$$

$$\frac{\partial\rho_{23}}{\partial t'} = -(\gamma_2 + i\Delta_2)\rho_{23} + iG_2(\rho_{33} - \rho_{22}) + iG_1^*\rho_{13},$$

$$\frac{\partial\rho_{33}}{\partial t'} = 2\gamma_2\rho_{22} - iG_2\rho_{32} + iG_2^*\rho_{23},$$

where the atomic detunings are given by $\Delta_1 = \omega_{12} - \omega_1$ and $\Delta_2 = \omega_{23} - \omega_2$, and $2\gamma_1$ and $2\gamma_2$ are the spontaneous emission rates from level $|1\rangle$ to level $|2\rangle$ and from level $|2\rangle$ to level $|3\rangle$, respectively. We have considered only the radiative relaxation processes in a dilute atomic gas active medium. All the frequency units are normalized with respect to the atomic decay γ_2, unless specified otherwise.

III. NUMERICAL MODELING AND STABILITY MAP

To understand the nonlinear dynamical aspects of this system, we solve the field Eq. (22), self-consistently with the atomic evolution given in Eqs. (25). Investigation of the nonlinear dynamics is carried out by computing the response (such as output fields x_i) for a given set of input fields y_1 and y_2, for a certain choice of atomic parameters (Δ_i, γ_i) and cavity parameters (θ_i, κ_i), and with the atom-cavity coupling governed by the cooperative parameters C_i. The Newton-Raphson method is used to obtain the solutions of the coupled nonlinear system of equations in the steady-state limit. The atom-field cavity interaction dictates the phases and amplitudes of both output fields. The multiplicity of the underlying solutions needs careful handling with regard to its numerical computation and is described in detail in the companion paper [13]. In essence, this system does not permit an *a priori* choice of both output fields, as is done conventionally to compute the corresponding input fields. An arbitrary choice of the output fields does not necessarily imply a physically realizable choice of the input fields.

Computations were undertaken using two independent numerical tools, one involving Fortran libraries associated with EISPACK [20] and the other using MATLAB. Furthermore, we also used the MATLAB continuation package MATCONT [21] to undertake the study of the nonlinear dynamical aspects of this system. We identify a series of fixed points that exhibit interesting bifurcations such as Hopf points, limit points, and period-doubling cascades in Fig. 4.

The unstable region and its neighborhood are quite often related to a variety of dynamical behavior such as periodic, quasiperiodic, or even chaotic dynamics, and hence a detailed bifurcation analysis was undertaken. Specifically, the periodic self-pulsing dynamics is further characterized by the Floquet multipliers that distinguish between stable and unstable limit cycles, and the Lyapunov exponents are calculated to identify and characterize chaotic behavior [22]. All these nonlinear dynamical features are independently confirmed by integrating the time-dependent equations Eqs. (22) and (25) using the fourth-order Runge-Kutta technique [23] under generic initial conditions, namely, atom in the ground state, $\rho_{33}(0) = 1$ [all

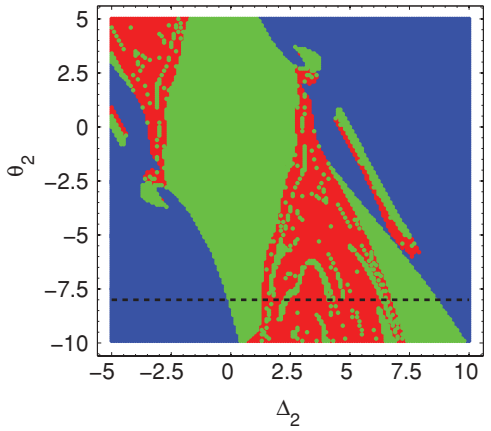

FIG. 2. (Color online) Stability domain map plotted between atomic detuning (Δ_2) and cavity detuning (θ_2). The stable fixed-point region (blue), the self-pulsing region (green), and the chaotic region (red) are indicated. Parameters are $\gamma_i = 1$, $\kappa_i = 1$, $\Delta_1 = 0$, $\theta_1 = 0$, $C_i = 200$, $|y_1| = 23$, and $|y_2| = 40$, for $i = 1,2$. The dashed line at $\theta_2 = -8$ indicates the specific parameter variation considered for the bifurcation study in Fig. 3. All the frequency quantities are in the units of γ_2^{-1}.

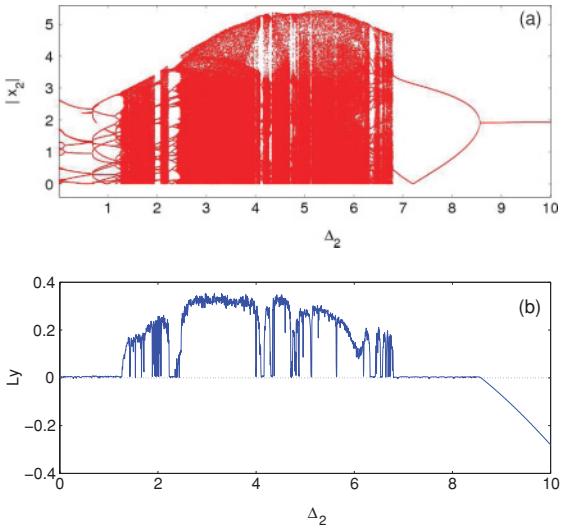

FIG. 3. (Color online) (a) Bifurcation diagram indicating the output field $|x_2|$; (b) the largest Lyapunov exponent (Ly) plotted with respect to atomic detuning Δ_2. Parameter values are the same as specified in Fig. 2 with $\theta_2 = -8$. All the frequency quantities are in the units of γ_2^{-1}.

other elements $\rho_{mn}(0) = 0$], and cavity output fields $x_i(0) = 0.01$, with varying values of the input fields y_i.

We present the highlights of the linear stability analysis in the form of the detailed stability map shown in Fig. 2. We believe the stability domain map will facilitate the experimental realization of these diverse nonlinear dynamical features. The parameter space associated with the system is exceedingly large owing to 12 physical parameters—$\gamma_{1,2}$, $\Delta_{1,2}$, $\theta_{1,2}$, $\kappa_{1,2}$, $C_{1,2}$, and $E^{\text{in}}_{1,2}$—each of which can be varied independently. The stability map in Fig. 2 indicates the range of just two of these parameters, Δ_2 and θ_2, and the system exhibits stable switching (blue region), periodic or quasiperiodic (green region), and chaotic (red region) dynamics. One can clearly see the islands of stable self-pulsing (green) within the chaotic region (red). The dashed (black) line indicates the dynamics that we explore further and is discussed below in detail along with the associated bifurcation diagram. The stability domain map allows one to pick up the appropriate parameter regime that corresponds to a desired dynamical behavior, such as self-pulsing, stable switching, or chaotic output; even complete avoidance of the chaotic region is possible by judicious choice of the trajectory in the multidimensional parameter space.

IV. NONLINEAR DYNAMICS

To understand the route to chaos we consider the bifurcation diagram along the dashed line in Fig. 2 and shown in Fig. 3(a). By varying the detuning Δ_2 while maintaining a constant cavity detuning ($\theta_2 = -8.0$), we obtain a period-doubling cascade for values of Δ_2 within [0:1.2] and inverse periodic doubling around $\Delta_2 \approx 8.5$. The largest Lyapunov exponent corresponding to the regions of self-pulsing is close to 0. The chaotic domains are clearly identified by the positive Lyapunov exponents as shown in Fig. 3(b). Self-pulsing and chaotic dynamics occur intermittently and the windows of stable periodic self-pulsing within a largely chaotic region are clearly shown. Beyond $\Delta_2 \approx 8.5$ all the Lyapunov exponents become negative, indicating that the system quickly moves toward a stable fixed-point behavior independent of the initial conditions; in our case this corresponds to stable switching.

We illustrate the input-output response and the associated nonlinear dynamical features for $|y_1| = 23$, as the other input field y_2 is varied. We obtain an S-shaped bistable response along with a hump-like feature. The associated linear stability analysis of the lower branch is also shown in Fig. 4; black(red) portions of the curves indicate unstable(stable) fixed points. The corresponding bistable curve without cavity feedback for the field coupling upper transition (systems with cooperative parameter $C_1 = 0$) is shown in the inset in Fig. 4 for comparison with the conventional OB.

The hump-like feature under an appropriate parameter regime transforms into a negative hysteretic bistable response.

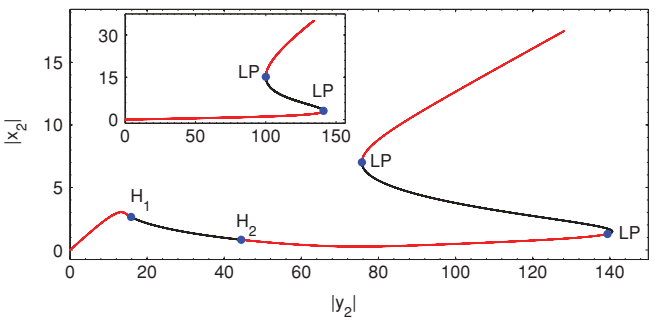

FIG. 4. (Color online) Bistable response having a hump-like feature for the field at ω_2 while the input field at ω_1 is held constant. The associated stable (red) and unstable (black) regions between the Hopf point (H_1, H_2) and the limit-point (LP) bifurcations are also indicated for $C_1 = 200$ and $C_2 = 200$, $|y_1| = 23$. Inset: Bistable response in the absence of feedback to field at ω_1 ($C_1 = 0$, $C_2 = 200$) with $|y_1| = 1.5$; other parameters are $\gamma_i = 1, \kappa_i = 1, \Delta_1 = 0, \theta_1 = 0$, $\Delta_2 = 4$, and $\theta_2 = -3$ for $i = 1,2$.

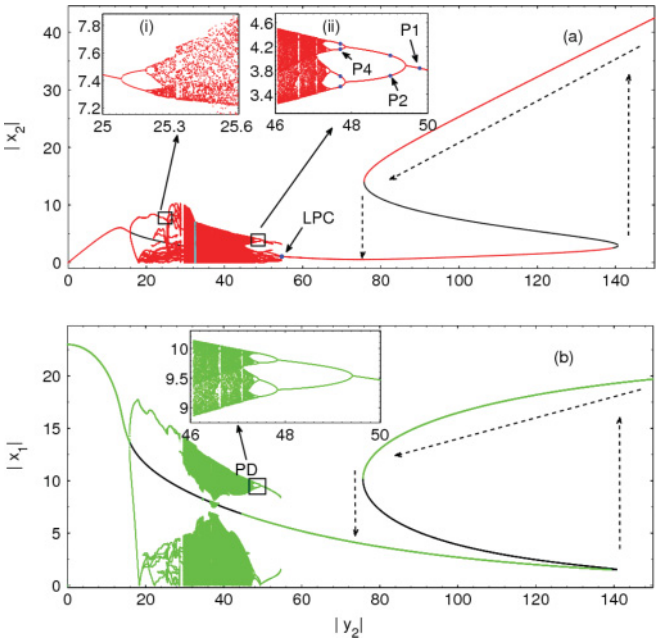

FIG. 5. (Color online) Bifurcation diagrams for the cavity output fields, indicating the periodic-doubling route to chaos. (a) Output field coupling the lower transition $|x_2|$ versus the input field $|y_2|$ and (b) output field coupling the upper transition $|x_1|$ versus $|y_2|$, for the same parameters as in Fig. 4. Unstable regions are shown in black.

The conventional hysteresis obtained in an OB system is considered to be positive, wherein at low input intensities the output is also low, and the system switches from a low-output state to a high-output state with increasing input field strength. However, in the region of the hump we obtain the opposite hysteretic response, wherein at low input intensities the output is high and the output switches to a lower value for higher input field strengths. Such a counterintuitive response encloses within it a negative hysteresis. The physical origin of the hump-like feature arises from the process of enhancement of the field at ω_2 arising as a result of suppressed absorption along the $|2\rangle \rightarrow |3\rangle$ transition [13]. The choice of a large cooperative parameter C_1 along the upper transition $|1\rangle \leftrightarrow |2\rangle$ leads to enhanced interaction of the atom with the ω_1 field and concurrently results in the extraction of a significant fraction of the population into excited states; specifically, the upper state $|1\rangle$ population increases. This leads to the creation of inversion along the upper transition $|1\rangle \leftrightarrow |2\rangle$ (i.e., $\rho_{11} > \rho_{22}$), resulting in a lowering of the influence of the field at ω_2 on these atoms and, thus, the accompanying suppressed absorption. This dynamics occurs due to the asymmetric choice of the cooperative parameters $C_1 > C_2$ under the cavity resonant condition $\theta_1 = \theta_2 = 0$. This inversion does not remain immune to a further increase in the field strength $|y_2|$ and the system exhibits conventional (positive) OB at higher input intensities.

Furthermore, the hump-like regime is also associated with nonlinear dynamical behavior arising due to cavity-assisted inversion as discussed above. The hump exhibits Hopf bifurcations, which are absent in conventional OB models involving feedback for one field (inset in Fig. 4). This feature is the result of an intricate interplay of phases of both fields; that is, if one demands that both the output fields are real, as done in Ref. [24], the hump-like feature as well as the nonlinear dynamical behavior disappears. We indicate bifurcation points such as Hopf points (H) and limit points (LP) in Fig. 4. In the unstable regime corresponding to the lower cooperative branch, one obtains self-pulsing as well as chaos at low input light levels. The bifurcation diagram associated with Fig. 4 is shown in Fig. 5. We also expand two illustrative

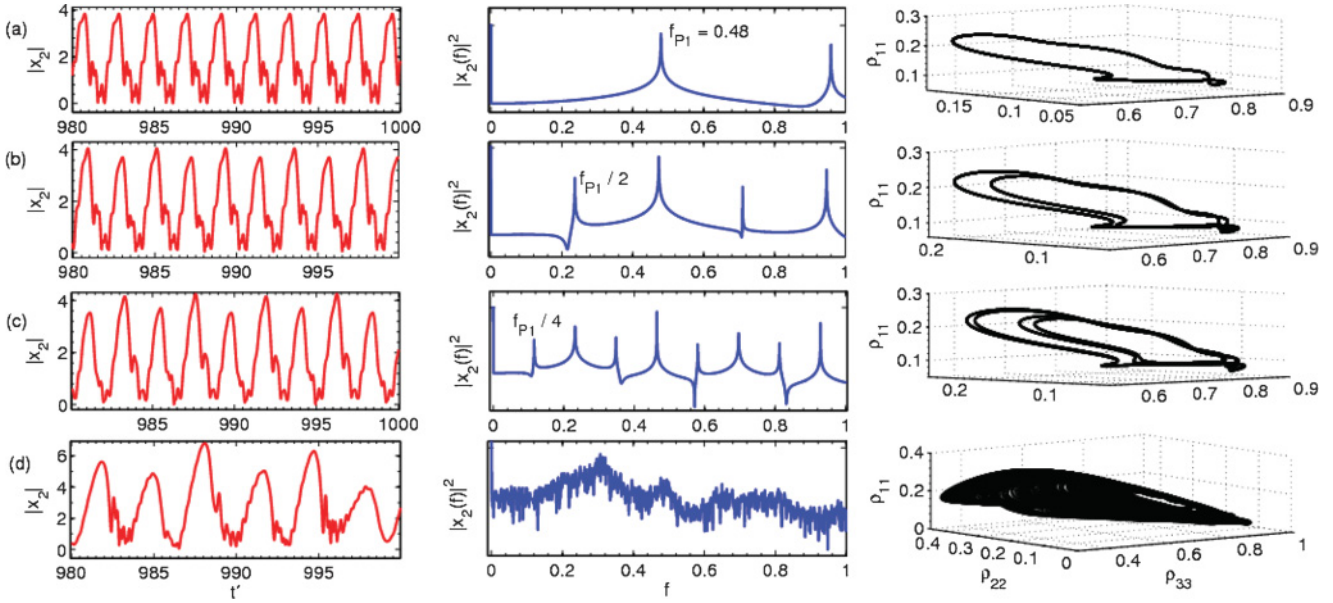

FIG. 6. (Color online) The time evolution of the output field (x_2) at ω_2 is shown in the first column, the corresponding spectrum (in arbitrary units) and the population phase plots (ρ_{11} versus ρ_{22} and ρ_{33}) are shown in the middle and the last columns, respectively. Plots in each row correspond to various values of the input field $|y_2|$ involved in the sequence of the period-doubling route ultimately leading to chaos: (a) period 1, with $|y_2| = 49.78$; (b) period 2, with $|y_2| = 49.01$; (c) period 4, with $|y_2| = 47.70$; and (d) chaos, with $|y_2| = 32.47$. Time t' is in the units of κ_1^{-1} and other parameters are the same as in Fig. 4.

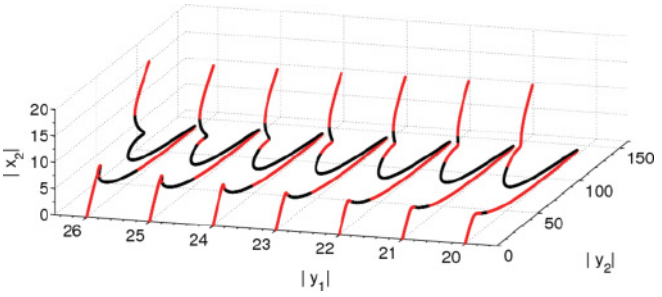

FIG. 7. (Color online) Development of negative hysteresis from the hump-like feature, as well as multistability for the field at ω_2 with $\Delta_1 = 4$, $\Delta_2 = 0$. Each curve corresponds to a particular value of the input field at ω_1, whose magnitude is varied from 20 to 30; the coexistence of three stable branches (multistability) is indicated in red. Other parameters are the same as in Fig. 4.

regions of the bifurcation diagram that indicate the onset of chaos. With increasing input field strength y_2 the system loses stability at the first Hopf point (H_1) and exhibits self-pulsing behavior. This is indicative of a supercritical Hopf bifurcation at H_1 [22]. The Hopf points indicate the onset of periodic behavior, and in between the Hopf points (H_1 and H_2) we observe a period-doubling route to chaos. The stability of the periodic behavior is established using Floquet multipliers, and chaos is confirmed using Lyapunov exponents as well as the output field spectrum.

There is a simultaneous existence of stable fixed-point solutions and self-pulsing limit cycles beyond the second Hopf point H_2 in the range (48:55). For this range of $|y_2|$, depending on the initial condition, the system can be driven to exhibit either periodic self-pulsing or regular stable switching. A transition from periodic behavior to the fixed-point solution occurs as a saddle-node/fold bifurcation that takes place beyond H_2 at $|y_2| = 54.6$, and is represented as the limit point of cycles (LPC) in Fig. 5. At the LPC two limit cycles (one stable and one unstable) coalesce and annihilate each other, leading to pure fixed-point solutions [22]. The stability of the limit cycles is indicated by the Floquet multipliers remaining within the unit circle, and transition out of the unit circle implies unstable limit cycles. Floquet multipliers associated with stable and unstable limit cycles (at $|y_2| = 51$ before

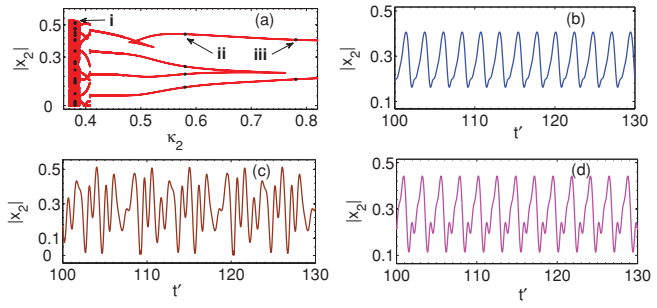

FIG. 8. (Color online) (a) Bifurcation diagram for the field at ω_2 as the cavity decay (κ_2) is tuned. Time evolution of output field for $\kappa_2 = 0.78$, $\kappa_2 = 0.30$, and $\kappa_2 = 0.58$, labeled as iii, i, and ii in (a) are presented in the panels (b),(c) and (d), respectively, for $C_1 = 1000$, $C_2 = 100$, $|y_1| = 25$, $|y_2| = 13$, $\theta_2 = 0$, $\Delta_2 = 0$. Time t' is in the units of κ_1^{-1} and other parameters are the same as in Fig. 2.

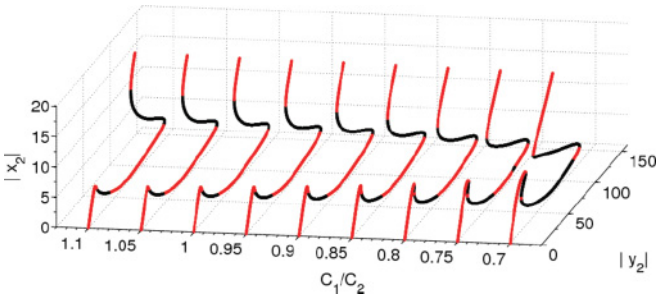

FIG. 9. (Color online) The hump-like feature progressively transforms into a negative hysteresis for comparable values of C_1 and C_2. Stable(unstable) regions are indicated in red(black). Parameters are the same as in Fig. 4.

they coalesce at LPC) are $0.3639 + i0$ and $-1.7997 + i0$ respectively.

The onset of chaos indicated in Fig. 5 occurs as one decreases the input field $|y_2|$ [see inset (ii)]. At first one obtains the self-pulsing output of period 1, which transforms into a self-pulsing output of period 2, period 4, and so on, as shown in Figs. 6(a)–6(c). The genesis of the new frequencies in the spectrum of the output field (second column) at $f_{P2} = f_{P1}/2$, $f_{P4} = f_{P1}/4$, and its multiples, apart from the dominant frequency $f_{P1} = 0.48$, clearly indicates a period-doubling route to chaos. Dashed arrows in Fig. 5 indicate conventional bistable switching. As both fields switch simultaneously, one can utilize this system for controllable switching at two distinct optical frequencies in optical communication applications. The period-doubling route to chaos is further substantiated by the three-dimensional phase plot (third column), involving the population of atomic states that show closed curves involving one, two, and four loops, respectively. As we decrease the input field $|y_2|$ further, to 32.47 [indicated by thick line with purple color in Fig. 5(a)], we obtain chaos and the corresponding two largest Lyapunov exponents are 0.3356 and 0.0031. The spectrum of the output field becomes continuous and the population phase plot gets filled up, clearly establishing the existence of chaos. This is also corroborated by the loss of stability of periodic behavior (limit cycles) [25] as reported in Table I, wherein the associated Floquet multipliers cross out of the unit circle along the negative real axis. Floquet multipliers having zero imaginary part and a transition out of the unit circle along the negative imaginary axis preclude the existence of quasiperiodicity, thus establishing a periodic-doubling route to chaos. The nonlinear dynamics of both fields closely resemble each other, and one obtains periodic self-pulsing to chaotic dynamics for both fields at ω_1 and ω_2, simultaneously.

This system offers a variety of control mechanisms, which allows one to access any desired dynamics by merely changing

TABLE I. Floquet multipliers for points P_1, P_2, and P_4, indicating the periodic-doubling cascade shown in inset (ii) in Fig. 5(a).

$\|y_2\|$	Period 1	Period 2	Period 4
49.78	$0.98 + 0i$	–	–
49.01	$-1.46 + 0i$	$0.99 + 0i$	–
47.70	$-2.58 + 0i$	$-1.77 + 0i$	$0.87 + 0i$

TABLE II. All frequency parameters are scaled with γ_2.

Parameter	Symbol	Range
Atomic detuning	$\Delta_{1,2}$	$-10 \leftrightarrow 10$
Cavity decays	$\kappa_{1,2}$	$0 \leftrightarrow 1$
Cavity detuning	$\theta_{1,2}$	$-10 \leftrightarrow 10$
Cooperative parameters	$C_{1,2}$	$100 \leftrightarrow 1000$
Input field strengths	$\lvert y_{1,2}\rvert$	$0 \leftrightarrow 150$

a few pertinent parameters. The inclusion of finite atomic detuning Δ_1 could even lead to multistability as shown in Fig. 7. A detailed analysis of multistable behavior will be presented elsewhere. We indicate other ways to control the stability as well as the nonlinear dynamical aspects in this system. One can obtain all the above-mentioned nonlinear dynamical features by varying the cavity decay κ_1 and/or κ_2. Such control over the nonlinear dynamical response is illustrated in the bifurcation diagram shown in Fig. 8, which involves κ_2 as the control parameter, which can be used to switch the chaotic dynamics on or off. It should be noted that the inclusion of finite cavity detuning (θ_2) aids in obtaining nonlinear dynamical features with values of the cooperative parameters C_1 and C_2 comparable to those shown in Fig. 9.

Before we conclude, we indicate the regime of operation in atomic vapor, such as rubidium, where these effects can be realized. Considering the ladder transition $5S_{1/2} \leftrightarrow 5P_{3/2} \leftrightarrow 5D_{5/2}$, at temperatures of about 60°C one would obtain a number density of $\approx 10^{11}$ atoms/cm^3. With the transmission coefficient $T \approx 10^{-2}$ the resulting cooperative parameter would be $C \approx 1000$. The input power levels could be varied from ≈ 0 to 20 mW across a spot size of 100 μm, and one would realize all the nonlinear dynamical effects as well as the conventional OB results discussed in this paper. The cooperative parameter can be varied further by changing either the number density of atoms or the transmission coefficient of the cavity. We also explicitly enumerate the range of parameters varied in this paper (see Table II).

V. CONCLUSIONS

We have demonstrated a new regime of nonlinear dynamical response at low input light levels for two-photon double-cavity OB with a three-level ladder atomic system as the active medium. Independent feedback is applied for both fields interacting with the atom. We present bifurcation diagrams that allow one to access the desired regime of nonlinear dynamical behavior. The system undergoes a period-doubling route to chaos in this new regime associated with the lower cooperative branch. A control paradigm based on careful maneuvering of parameters so as to traverse across phase space in order to obtain *any* desired dynamics is demonstrated through the stability map. The system exhibits a negative as well as a positive hysteresis bistable response, stable periodic self-pulsing, and chaotic dynamics, apart from multistability and conventional switching.

ACKNOWLEDGMENTS

We gratefully acknowledge the help provided by Drs. Supriyo Pal, Pankaj Wahi, and M. K. Verma, particularly with regard to the nonlinear dynamical aspects of this work. One of us (H.A.B.) would like to thank the Indian Institute of Technology Kanpur, India for financial support.

[1] J. T. Gleeson, Appl. Phys. Lett. **81**, 1949 (2002).
[2] T. Stojanovski, J. Pihl, and L. Kocarev, IEEE Trans. Circuits Syst. I **48**, 382 (2001).
[3] G. M. Maggio, N. F. Rulkov, and L. Reggiani, IEEE Trans. Circuits Syst. I **48**, 1424 (2001).
[4] S. Sivaprakasam and K. A. Shore, Opt. Lett. **24**, 466 (1999).
[5] G. D. VanWiggeren and R. Roy, Science **279**, 1198 (1998).
[6] H. M. Gibbs, *Optical Bistability: Controlling Light with Light* (Academic Press, New York, 1985).
[7] L. A. Lugiato, *Progress in Optics*, edited by E. Wolf (North-Holland, Amsterdam, 1984), Vol. XXI, p. 69.
[8] K. Ikeda, H. Daido, and O. Akimoto, Phys. Rev. Lett. **45**, 709 (1980).
[9] L. A. Lugiato, V. Benza, L. M. Narducci, and J. D. Farina, Opt. Commun. **39**, 405 (1981).
[10] J. Amitabh and X. Min, J. Mod. Opt. **57**(14), 1196 (2010).
[11] R. Bonifacio and L. A. Lugiato, Opt. Commun. **19**, 172 (1976).
[12] R. Bonifacio and L. A. Lugiato, Lett. Nuovo Cimento **21**, 510 (1978).
[13] H. Aswath Babu and H. Wanare, preceding paper, Phys. Rev. A **83**, 033818 (2011).
[14] H. Haken, Phys. Lett. **53**, 77 (1975).
[15] L. A. Orozco, H. J. Kimble, A. T. Rosenberger, L. A. Lugiato, M. L. Asquini, M. Brambilla, and L. M. Narducci, Phys. Rev. A **39**, 1235 (1989).
[16] S. M. A. Maize, Chaos Solitons Fractals **28**, 590 (2006).
[17] C. M. Savage, H. J. Carmichael, and D. F. Walls, Opt. Commun. **42**, 3 (1982).
[18] P. Grangier, J. F. Roch, J. Roger, L. A. Lugiato, E. M. Pessina, G. Scandroglio, and P. Galatola, Phys. Rev. A **46**, 2735 (1992).
[19] W. Yang, A. Joshi, and M. Xiao, Phys. Rev. Lett. **95**, 093902 (2005).
[20] B. T. Smith, J. M. Boyle, J. J. Dongarra, B. S. Garbow, Y. Ikebe, V. C. Klema, and C. B. Moler, *Matrix Eigensystem Routines—EISPACK Guide* (LNCS, Springer, Heidelberg, 1976), Vol. 6.
[21] A. Dhooge, W. Govaerts, and Yu. A. Kuznetsov, ACM Trans. Math. SoftwareACMSCU **29**, 141 (2003). The MATCONT package is available at [http://www.matcont.ugent.be].
[22] S. H. Strogatz, *Nonlinear Dynamics and Chaos* (Perseus Books, New York, 1994).
[23] W. H. Press, S. A. Teukolsky, W. T. Vetterling, and B. P. Flannery, *Numerical Recipes in Fortran* (Narela, Delhi, 1998).
[24] A. Joshi and M. Xiao, Appl. Phys. B **79**, 65 (2004).
[25] Yu. A. Kuznetsov, *Elements of Applied Bifurcation Theory* (Springer-Verlag, New York, 1998).